ESTIMATING SEISMIC DISPERSION FROM PRESTACK DATA USING FREQUENCY-DEPENDENT AVO ANALYSIS

XIAOYANG WU[1], MARK CHAPMAN[1,2] and XIANG-YANG LI[1]

1 Edinburgh Anisotropy Project, British Geological Survey, Murchison House, West Mains Road, Edinburgh EH9 3LA, U.K. xywu@bgs.ac.uk
2 School of Geosciences, University of Edinburgh, The King's Buildings, West Mains Road, Edinburgh EH9 3JW, U.K.

(Received January 16, 2014; revised version accepted May 10, 2014)

ABSTRACT

Wu, X., Chapman, M. and Li, X.-Y., 2014. Estimating seismic dispersion from prestack data using frequency-dependent AVO analysis. *Journal of Seismic Exploration*, 23: 219-239.

Recent laboratory measurement studies have suggested a growing consensus that fluid saturated rocks can have frequency-dependent properties within the seismic bandwidth. It is appealing to try to use these properties for the discrimination of fluid saturation from seismic data. In this paper, we develop a frequency-dependent AVO (FAVO) attribute to measure magnitude of dispersion from pre-stack data. The scheme essentially extends the Smith and Gidlow's (1987) two-term AVO approximation to be frequency-dependent, and then linearize the frequency-dependent approximation with Taylor series expansion. The magnitude of dispersion can be estimated with least-square inversion. A high-resolution spectral decomposition method is of vital importance during the implementation of the FAVO attribute calculation. We discuss the resolution of three typical spectral decomposition techniques: the short term Fourier transform (STFT), continuous wavelet transform (CWT) and Wigner-Ville Distribution (WVD) based methods. The smoothed pseudo Wigner-Ville Distribution (SPWVD) method, which uses smooth windows in time and frequency domain to suppress cross-terms, provides higher resolution than that of STFT and CWT. We use SPWVD in the FAVO attribute to calculate the frequency-dependent spectral amplitudes from pre-stack data. We test our attribute on forward models with different time scales and crack densities to understand wave-scatter induced dispersion at the interface between an elastic shale and a dispersive sandstone. The FAVO attribute can determine the maximum magnitude of P-wave dispersion for dispersive partial gas saturation case; higher crack density gives rise to stronger magnitude of P-wave dispersion. Finally, the FAVO attribute was applied to real seismic data from the North Sea. The result suggests the potential of this method for detection of seismic dispersion due to fluid saturation.

KEY WORDS: frequency dependent AVO, spectral decomposition, prestack, seismic dispersion.

0963-0651/14/$5.00

INTRODUCTION

Frequency-dependent attenuation and dispersion are attracting more and more interests because they are believed to be directly associated to rock properties such as scale length of heterogeneities, rock permeability and saturating fluid. Theoretical studies of rock physics models (White, 1975; Chapman et al., 2003; Müller and Rothert, 2006; Gurevich et al., 2009) and Laboratory measurements of fluid saturated rocks (Murphy, 1982; Gist, 1994; Quintal and Tisato, 2013) suggested that wave-induced fluid flow between mesoscopic-scale heterogeneities is a major cause of P-wave attenuation and velocity dispersion in partially saturated porous media.

Since seismic attenuation is more sensitive to rock properties than velocity dispersion is, direct Q value estimation and tomography have been widely studied as a seismic attribute for reservoir characterization. The classical spectral ratio (Bath, 1974; Hauge, 1981; Dasgupta and Clark, 1998; Taner and Treitel, 2003) utilizes the ratio of seismic amplitude spectra at two different depths varies as a function of frequency to estimate Q value. Central frequency shift method (Quan and Harris, 1997) calculates Q from the decrease in centroid frequency of a spectrum of seismic wave traveling through a lossy medium.

The amplitude-versus-offset (AVO) as a lithology and fluid analysis tool has been utilized for over twenty years. However, the AVO theory is based on Zoeppritz equation and Gassmann's theory, in which attenuation and dispersion is generally not accounted for. Application of spectral decomposition techniques allows the frequency-dependent AVO behavior due to fluid saturation to be detected on seismic data, because reflections from hydrocarbon-saturated zone are thought to have a tendency of being low-frequency (Castagna et al., 2003).

Chapman et al. (2006) performed a theoretical study of reflections from the interface between a layer which exhibits fluids-related dispersion and an elastic overburden, and showed that in such cases the AVO response was frequency-dependent. Class I reflections tend to be shifted to higher frequency while class III reflections have their lower frequencies amplified. Recently, the frequency-dependent AVO (FAVO, Wilson et al., 2009; Wilson, 2010) inversion is introduced in an attempt to allow a quantitative measure of dispersion to be derived from pre-stack data. In this paper, we test the FAVO inversion scheme on synthetic and real seismic data to obtain a FAVO attribute. We begin by mathematically formulating the FAVO inversion theory based on Smith and Gidlow's (1987) two-term AVO approximation. Then the resolution of three typical spectral decomposition techniques: the short term Fourier transform (STFT), continuous wavelet transform (CWT) and the smoothed pseudo Wigner-Ville Distribution (SPWVD) based methods, have been discussed. The SPWVD with higher resolution is used to calculate the frequency-dependent spectral amplitudes from pre-stack data. We also discuss the effect of time scale parameter that control the frequency dispersion regime and crack density on the magnitude of dispersion estimation. Finally, the FAVO attribute is applied to seismic data from the North Sea.

FAVO ATTRIBUTE FOR SEISMIC DISPERSION

Linear approximations to the exact Zoeppritz reflection coefficients can provide useful insights into subsurface properties. Smith and Gidlow's (1987) removed the density variation ($\Delta\rho/\rho$) from Aki and Richards (1980) by using Gardner et al., (1974) relationship between density and P-wave velocity for water-saturated rocks. Then the approximation becomes two-terms and the P- and S-wave reflectivities ($\Delta V_P/V_P$ and $\Delta V_S/V_S$) can be inverted using parameters that are either known or can be estimated with Least-Square inversion. The reflection coefficient R of Smith and Gidlow's (1987) approximation can be written as:

$$R(\theta) \approx A(\theta)(\Delta V_P/V_P) + B(\theta)(\Delta V_S/V_S) \quad , \tag{1}$$

where θ is the angle of incidence, the two offset-dependent constants A and B can be derived in terms of V_P, V_S, and the angle of incidence (θ_i) which can be calculated by way of ray tracing. Following the theory of Wilson et al.(2010), the coefficients A and B are frequency-independent and do not vary with velocity dispersion, the reflection coefficient R and the P- and S-wave reflectivities $\Delta V_P/V_P$ and $\Delta V_S/V_S$, are considered to vary with frequency due to attenuation and dispersion at the interface or through the hydrocarbon saturated reservoir, then (1) can be written as:

$$R(\theta,f) \approx A(\theta)(\Delta V_P/V_P)(f) + B(\theta)(\Delta V_S/V_S)(f) \quad . \tag{2}$$

Expanding (2) as first-order Taylor series around a reference frequency f_0:

$$R(\theta,f) \approx A(\theta)(\Delta V_P/V_P)(f_0) + (f - f_0)A(\theta)I_a$$
$$+ B(\theta)(\Delta V_S/V_S)(f_0) + (f - f_0)B(\theta)I_b \quad , \tag{3}$$

where I_a and I_b are the derivatives of P- and S-wave reflectivities with respect to frequency evaluated at f_0:

$$I_a = (d/df)(\Delta V_P/V_P) \; ; \; I_b = (d/df)(\Delta V_S/V_S) \quad . \tag{4}$$

For a typical CMP gather with n receivers denoted as a data matrix s(t,n). Coefficients A and B at each sampling point, denoted as $A_n(t)$ and $B_n(t)$, can be derived with the knowledge of velocity model through ray tracing. Spectral decomposition is performed on s(t,n) to derive the spectral amplitude S(t,n,f) at a series of frequencies. However, S contains the overprint of seismic wavelet, so we perform spectral balance, by which the spectral amplitudes at different frequencies are matched to the spectral amplitude at the reference frequency f_0 through a strong continuous reflection caused by elastic interface, to remove this effect with a suitable weight function w(f,n):

$$D(t,n,f) = S(t,n,f)w(f,n) \quad . \tag{5}$$

where D(t,n,f) is the balanced spectral amplitude. w(f,n) is calculated from a defined window with k sampling points using the ratio of RMS amplitudes at the chosen reference frequency f_0 and other frequencies as shown in (6),

$$w(f,n) = [\sqrt{\{\sum_k S^2(t,n,f_0)\}}]/[\sqrt{\{\sum_k S^2(t,n,f)\}}] \quad . \tag{6}$$

Giving the fact that the seismic amplitudes can be associated with the reflection coefficients through convolution with a seismic wavelet in the AVO analysis. The relationship between spectral amplitude and reflectivity depends on the spectral decomposition we used. According to (2), we derive $\Delta V_P/V_P$ and $\Delta V_S/V_S$ at the reference frequency f_0 by replacing R with D. Considering m frequencies $[f_1, f_2, \ldots f_m]$, eq. (3) can be expressed as matrix form:

$$\begin{bmatrix} D(t,1,f_1)-A_1(t)(\Delta V_P/V_P)(f_0,t)-B_1(t)(\Delta V_S/V_S)(f_0,t) \\ \vdots \\ D(t,1,f_m)-A_1(t)(\Delta V_P/V_P)(f_0,t)-B_1(t)(\Delta V_S/V_S)(f_0,t) \\ \vdots \\ D(t,n,f_1)-A_n(t)(\Delta V_P/V_P)(f_0,t)-B_n(t)(\Delta V_S/V_S)(f_0,t) \\ \vdots \\ D(t,n,f_m)-A_n(t)(\Delta V_P/V_P)(f_0,t)-B_n(t)(\Delta V_S/V_S)(f_0,t) \end{bmatrix} \approx \begin{bmatrix} (f_1-f_0)A_1(t) & (f_1-f_0)B_1(t) \\ \vdots & \vdots \\ (f_m-f_0)A_1(t) & (f_m-f_0)B_1(t) \\ & \vdots \\ (f_1-f_0)A_1(t) & (f_1-f_0)B_n(t) \\ \vdots & \vdots \\ (f_m-f_0)A_n(t) & (f_m-f_0)B_n(t) \end{bmatrix} \begin{bmatrix} I_a \\ I_b \end{bmatrix} . \tag{7}$$

which can be denoted as:

$$RR = RM \begin{bmatrix} I_a \\ I_b \end{bmatrix} \quad . \tag{8}$$

Then the attributes of I_a and I_b can be calculated with least-squares-inversion:

$$\begin{bmatrix} I_a \\ I_b \end{bmatrix} = (RM^T RM)^{-1} RM^T RR \quad . \tag{9}$$

CHOICE OF SPECTRAL DECOMPOSITION TECHNIQUES

Application of spectral decomposition techniques allows the frequency-dependent AVO behaviour to be detected from seismic data. A high resolution method is of vital importance for the accuracy and robustness of estimating seismic dispersion. Here we study and compare three different spectral decomposition techniques: short-time Fourier transform (STFT), continuous wavelet transform (CWT) and Wigner-Ville distribution (WVD) based method. The STFT introduced by Gabor (1946) can be expressed as,

$$\mathrm{STFT}(t,f) = \langle x(\tau), \varphi(\tau-t)e^{j2\pi f\tau} \rangle = \int_{-\infty}^{\infty} x(\tau)\bar{\varphi}(\tau-t)e^{-j2\pi f\tau}d\tau \ , \qquad (10)$$

where φ is the window function centred at time $\tau = t$, and $\bar{\varphi}$ is the complex conjugate of φ. The STFT is a type of linear Time-Frequency Representation (TFR). The choice of the width of window functions leads to a trade-off between time localization and frequency resolution (Cohen, 1989).

As shown in Fig. 1, the signal consists of two quadratic FM signals with different frequency components. The frequency increases with time in quadratic trend, while the amplitude keep unchanged. We use the regularly used window functions: Hamming window, Hanning window, Gauss window and Nuttall window for STFT spectral analysis, for which the expression of window functions are as follows:

Hamming window: $w(n) = 0.54 - 0.46 \times \cos(2\pi n/N), \quad 0 \le n \le N;$

Hanning window: $w(n) = 0.5[1 - \cos(2\pi n/N)], \quad 0 \le n \le N;$

Gauss window: $w(n) = e^{-\frac{1}{2}[\alpha n/(N/2)]^2}, \quad -(N/2) \le n \le (N/2)$, the length of the window is $N+1$;

Nuttall window: $w(n) = a_0 - a_1 \times \cos(2\pi n/N) + a_2 \times \cos(4\pi n/N) - a_3 \times \cos(6\pi n/N), \quad 0 \le n \le N;$

where $a_0 = 0.3635819$; $a_1 = 0.4891775$; $a_2 = 0.1365995$; $a_3 = 0.0106411$.

The shapes of the four window functions are shown in Fig.2. The Hamming window and Hanning window are wider than the Gauss and Nuttall windows.

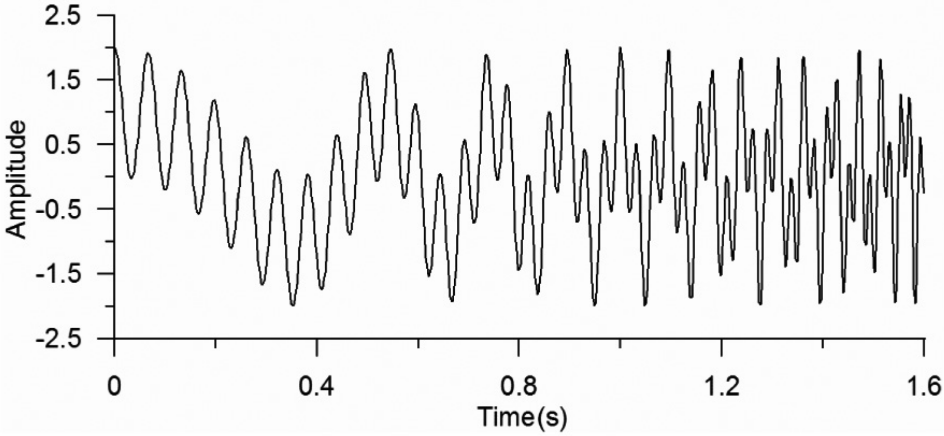

Fig. 1. Quadratic FM signal comprised of two frequency components. The frequency of the signal increases with time.

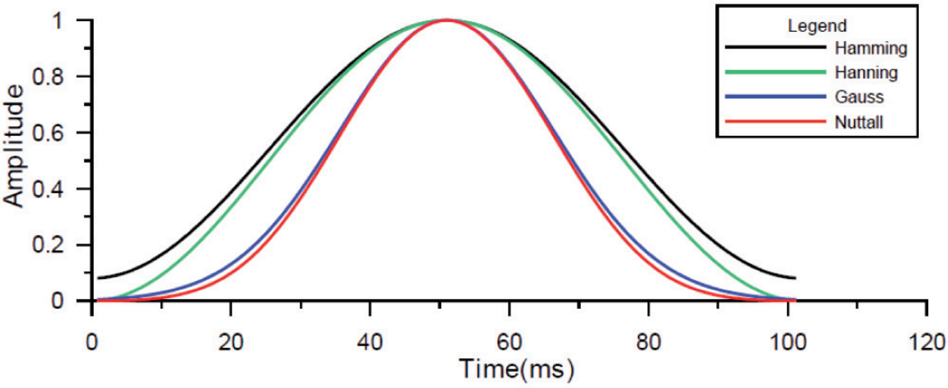

Fig. 2. The shapes of four different window functions. The Gaussian and Nuttall windows are wider than Hamming and Hanning windows.

Fig. 3 displays the STFT spectra with the four different window functions. The spectra with the Hamming window and Hanning window have higher frequency resolution especially at low frequencies but low temporal resolution as indicated by the stripes between the two signal components; while the Gauss window and Nuttall window show high temporal resolution especially at high frequency but relatively low frequency resolution at low frequency. However, we can see that Gauss and Nuttall windows provide a better TFR than Hamming and Hanning windows for this signal.

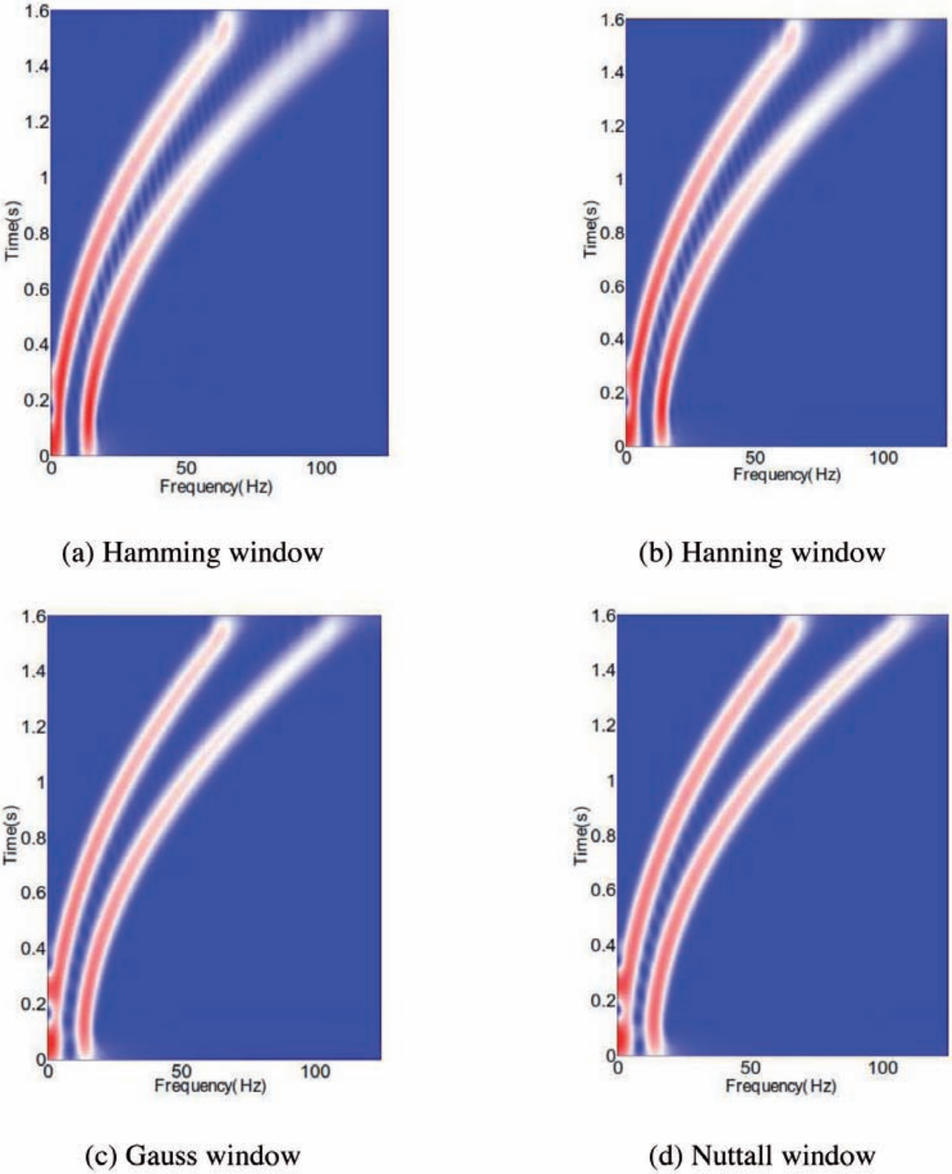

Fig. 3. STFT spectra with different window functions. The spectra using Gauss and Nuttall windows have higher temporal resolution than that of using Hamming and Hanning (Windowslength: 400 ms).

The Continuous Wavelet Transform of a signal s(t) is defined as the inner product of a family of wavelets $\psi_{a,b}(t)$ and s(t) (Mallat, 1993; Sinha et al., 2005):

$$S(a,b) = \langle\, s(t), \psi_{a,b}(t) \,\rangle = (1/\sqrt{|a|}) \int_{-\infty}^{\infty} s(t)\psi[(t-b)/a]dt \quad , \qquad (11)$$

where a is the dilation parameter (corresponding to frequency information), b is the translation parameter (corresponding to temporal information), $\psi(t)$ is the complex conjugate of $\psi(t)$, S(a,b) is the variation of the original signal s(t) with the observation area under different scales at time t = b.

Consider another hyperbolic FM signal with two different frequencies as shown in Fig. 4. A 400 ms Hamming window is used for STFT and the Morlet wavelet is used for CWT to obtain time-frequency spectra as shown in Fig. 5. From Fig. 5 (a), we can see STFT spectrum displays high resolution at low frequencies but low resolution at high frequencies due to a predefined window size. Fig. 5(b) is the result of CWT, we can see the event is thinner than that of STFT. Frequency resolution at low frequencies is improved. Temporal resolution at high frequency is significantly improved as well due to the dilation of wavelet function.

A third time-frequency representation in seismic signal analysis is the Wigner-Ville distribution (WVD, Claasen and Mecklenbrücker, 1980; Cohen, 1989). The WVD of the signal x(t) can be defined as,

$$WVD(t,f) = \int_{-\infty}^{\infty} X(t + \tau/2)\bar{X}(t - \tau/2)e^{-j2\pi f\tau}d\tau \quad , \qquad (12)$$

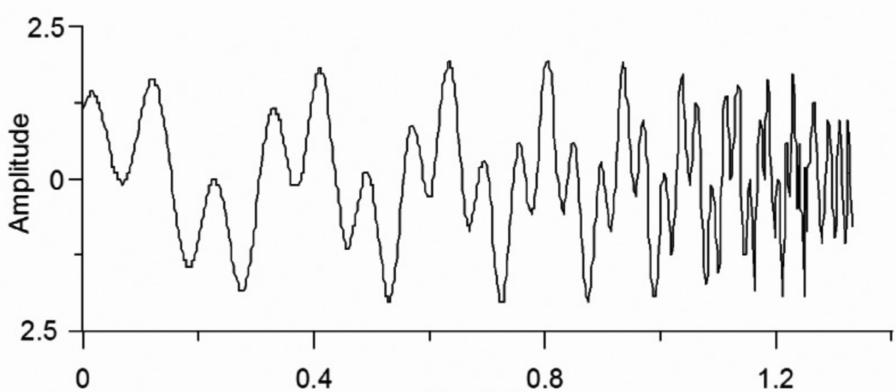

Fig. 4. Hyperbolic FM signal with two frequency components. The frequency of the signal becomes higher with increase of time.

where τ is the time delay variable, X(t) is the analytical signal associated with the real signal x(t),

$$X(t) = x(t) + jH[x(t)] \quad . \tag{13}$$

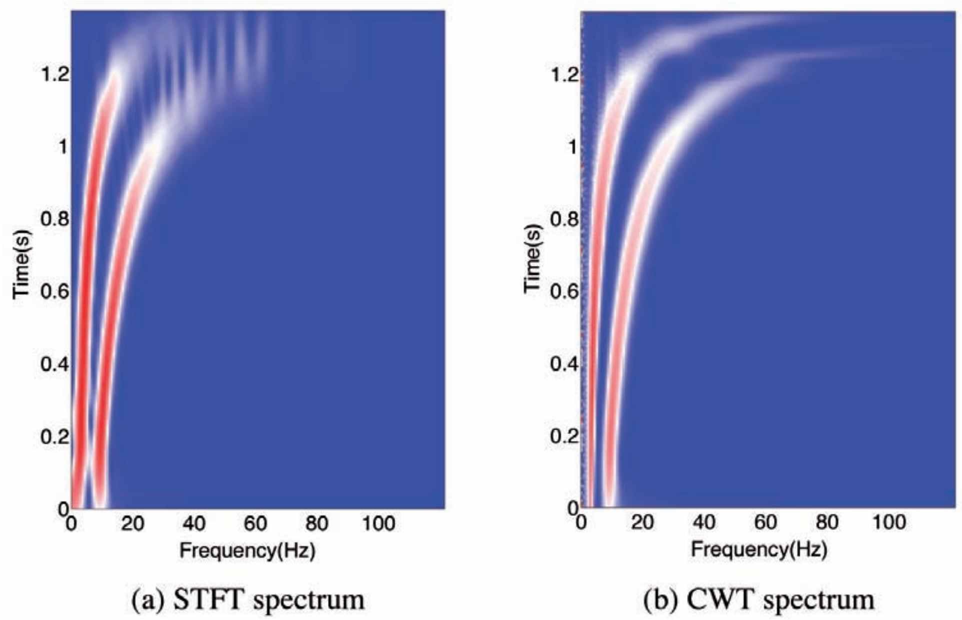

Fig. 5. Comparison of STFT and CWT spectra for the FM signal in Fig. 4.

H[x(t)] is the Hilbert transform of x(t) as the imaginary part of X(t). The WVD avoids the STFT trade-off between time and frequency resolution. However, this improvement comes at the cost of the well-known cross-term interference (CTI) caused by WVD bilinear characteristic. One of the improvements is the smoothed pseudo Wigner-Ville distribution (SPWVD), using both a time smoothing window and a frequency smoothing window independently, expressed as

$$SW_{g,h,X}(t,f) = \int_{-\infty}^{\infty}\int_{-\infty}^{\infty} X(t + \tau/2)\bar{X}(t - \tau/2)g(\nu)h(\tau)e^{-j2\pi f\tau}d\nu d\tau \quad , \tag{14}$$

where ν is the time delay and τ is the frequency offset. $g(\nu)$ is the time smoothing window, $h(\tau)$ the frequency smoothing window on condition that $g(\nu)$

and h(τ) are both real symmetric functions and g(0) = h(0). Then it is possible to attenuate the CTI presented in the WVD, by independently choosing the type of these two windows.

As shown in Fig. 6, a synthetic seismic trace comprised of three components is constructed by adding Ricker wavelets of different centre frequencies. We perform SPWVD with a 30 ms and a 60 ms length Gauss low-pass filter as a time and frequency smoothing window, STFT with a 80 ms length Hamming window and CWT with Morlet wavelet respectively. We can see the SPWVD method provides the highest resolution, while both temporal and frequency resolutions are not high enough to demonstrate the spectral characteristics with STFT method. The CWT result shows that the temporal resolution is high but the frequency resolution is low at low frequencies, and the frequency resolution is high but the temporal resolution is low at high frequencies. We use the SPWVD for spectral decomposition of prestack data in the FAVO attribute estimation.

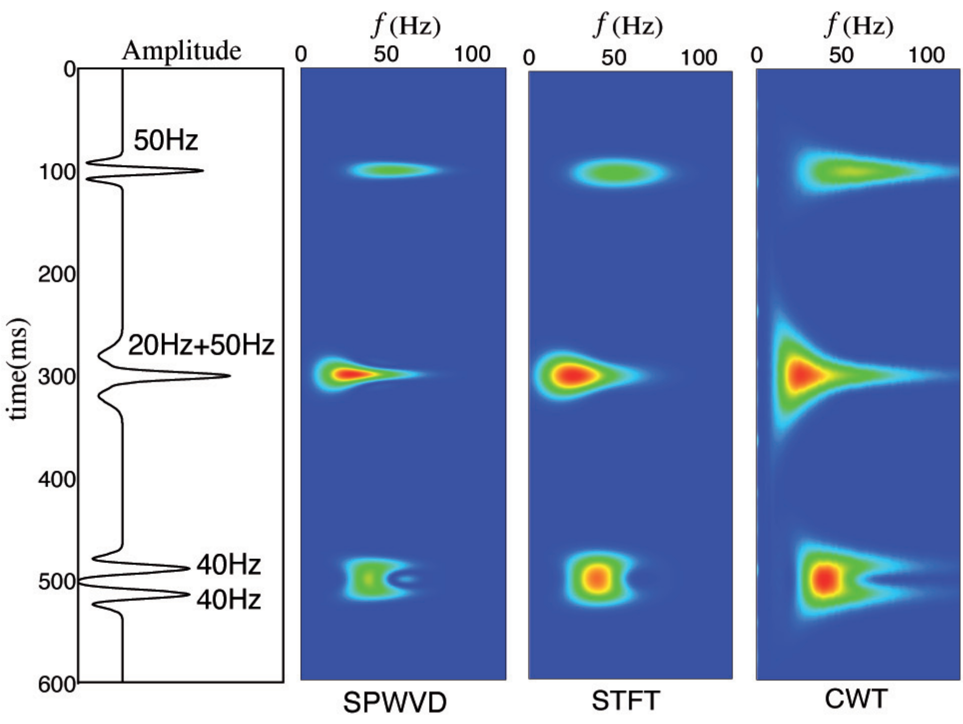

Fig. 6. A synthetic trace constructed by Ricker wavelets of different centre frequencies and its spectra generated with different methods. The SPWVD shows superior resolution than STFT and CWT method for this signal.

NUMERICAL MODELLING OF DISPERSION ESTIMATION

We study a case that considers the effect of variation of timescale t on the magnitude of dispersion caused by scattering at the interfaces. Timescale t controls the frequency range over which dispersion occurs. The choice of material parameters is based on the models created by Chapman et al. (2006). The case is a two-layer model, in which the top elastic shale has P- and S-wave velocities of 2743 m/s and 1394 m/s, and a density of 2.06 g/cm^3. The lower sandstone is considered to have a P- and S-wave velocities of 2835 m/s and 1472 m/s, and a density of 2.08 g/cm^3 under water saturation and then change to partial gas saturation with wood equation to calculate the mixed fluid moduli. The parameters of the model are listed in Table 1.

Table 1. Material parameters for the two-layer model as described in Chapman et al. (2006).

Lithofacies	V_P(m/s)	V_S(m/s)	ρ_W(g/cm^3)	ρ_G(g/cm^3)	φ(%)	cd(%)	Thickness(m)
Shales	2743	1394	2.06	-	-	-	1000
Sandstone	2835	1472	2.08	2.04	15	5	Half space

11 receivers were synthesized with a trace spacing of 100 m and 40 Hz Ricker wavelet as the explosive source. Fig. 7 displays the four synthetic gathers generated by ANISEIS software package with a Fortran program to create the frequency dependent layer. Two dispersive cases have the same τ value of 5×10^{-3} s under water and partial gas saturation, respectively. Such a τ value corresponds to the transition frequency being located at the seismic band. The low frequency case ($\tau = 1\times10^{-6}$ s) and the high frequency case ($\tau = 100$ s) have no attenuation and correspond to elastic case. From Fig. 7(a), we can see the typical Class I AVO feature that the amplitudes decrease with offset under water saturation. However, Class I AVO changes to Class III AVO when the fluid is substituted with partial gas saturation. Another feature when partial gas saturation is that the amplitudes decrease with increasing τ value. This indicates the reduction of velocity difference and acoustic impedance difference between the two layers from low frequency to high frequency.

Using 40 Hz (dominant frequency of the source wavelet) as the reference frequency, we calculate the FAVO attribute with the spectral amplitudes at a series of frequencies 25 Hz, 30 Hz, 40 Hz, 50 Hz, 60 Hz, 70 Hz and 80 Hz. A set of weights were derived in the elastic model by matching the maximum spectral amplitude at non-reference frequencies to the maximum spectral amplitude at 40 Hz. These same weights are applied to the dispersive model to remove the wavelet overprint. Since the shear modulus is decoupled from the saturating fluids, we only calculate the derivative of P-wave reflectivity I_a. Fig.8 displays a comparison between the balanced isofrequency sections at 25 Hz, 50 Hz and 80 Hz for the two dispersive models under water and partial gas saturation, respectively. We can see that for partial gas, energy decreases with increasing frequency, whereas energy increases with increasing frequency when saturated with water.

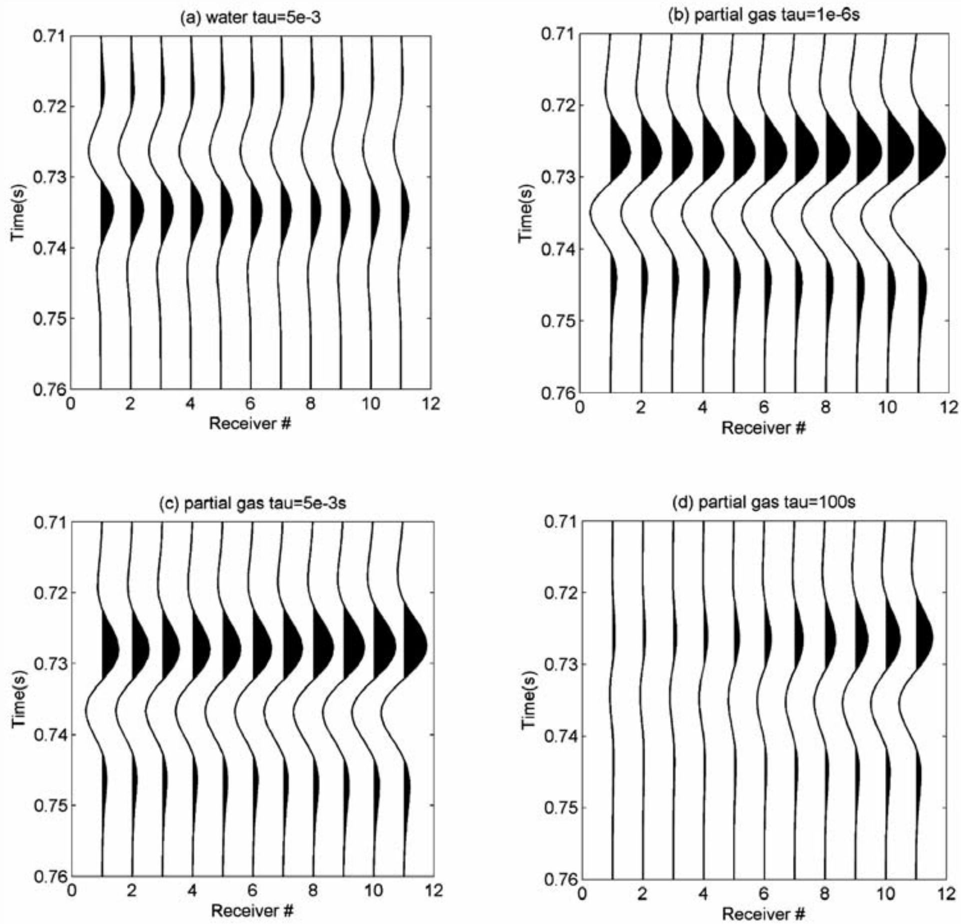

Fig. 7. Four synthetic gathers under full water saturation when (a): $\tau = 5\times10^{-3}$ s, and partial gas saturation when (b): $\tau = 1\times10^{-6}$ s, (c): $\tau = 5\times10^{-3}$ s and (d): $\tau = 100$ s.

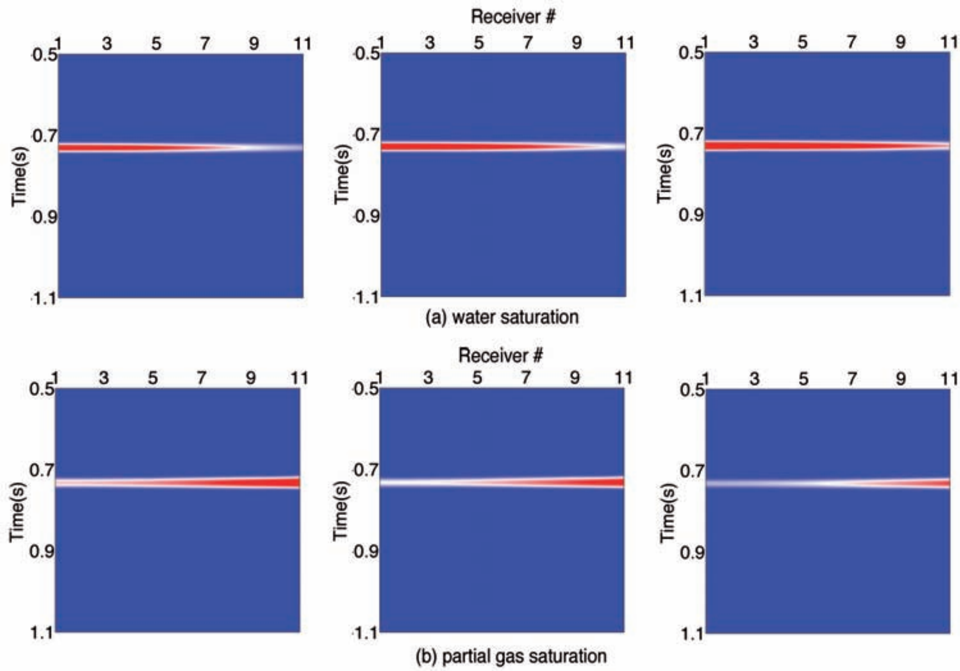

Fig. 8. Isofrequency sections at 25 Hz, 50 Hz and 80 Hz for the dispersive models under water and partial gas saturation, respectively ($\tau = 5\times10^{-3}$ s).

Fig. 9. displays the I_a attribute for the four models. We can see that the magnitude of P-wave dispersion for the partial gas saturation when $\tau = 5\times10^{-3}$ s (c) is the highest. This is much more significant than low and high frequency cases (b and d), of which there is almost no dispersion occurring. The result for dispersive model under water saturation (a) is a little weak compared with (c), indicating the magnitude of dispersion is weaker than partial gas saturation. This can be seen from the isofrequency sections.

Fig. 10 displays the reflection coefficients varying with angle of incidence at frequencies 25, 30, 40, 50, 60, 70 and 80 Hz under the two dispersive models (Figs. 7a and 7c). Comparing the amount of separation between the curves of different frequencies, we can see that there is stronger dispersion within the seismic bandwidth in the synthetic seismogram under partial gas saturation. This corresponds to the result displayed in Fig. 9.

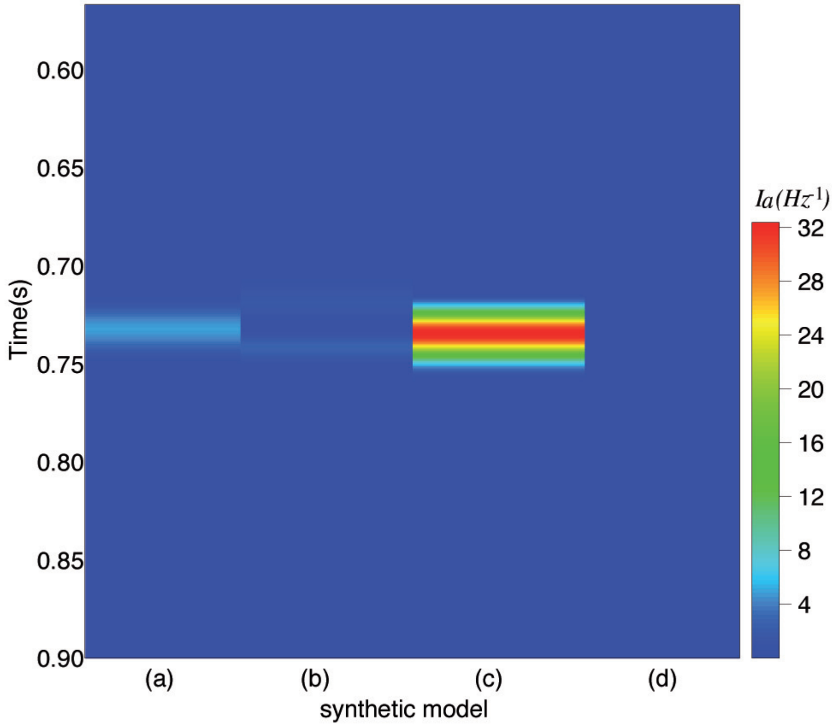

Fig. 9. The attribute of derivative of P-wave reflectivity I_a for the four synthetics models as displayed in Fig. 7.

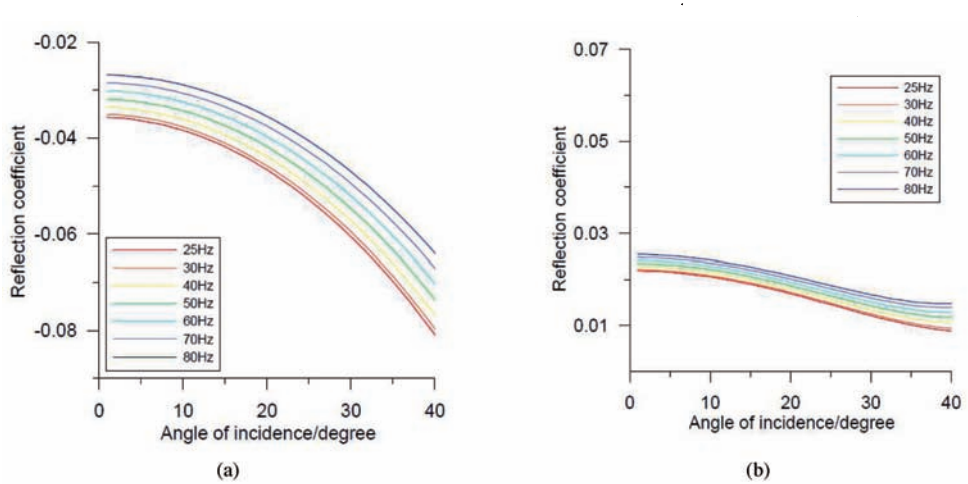

Fig. 10. The P-wave reflection coefficient versus angle of incidence for the two dispersive model under water and partial gas saturation, respectively. (a) partial gas saturation; (b) water saturation.

In the second case we create a three-layer model with varying crack densities of 5%, 10%, 15% and 20% for the dispersive sandstone under gas saturation, in order to study the influence of crack density on the magnitude of dispersion. The P-wave and S-wave velocity and density are the same as that of the previous example, but an elastic overburden shale layer is added to form an elastic interface for spectral balance. All the parameters are listed in Table 2. Using 40 Hz Ricker wavelet as the source, we create the four models with 4 receivers (1.1 - 1.4 km) at a trace spacing of 100 m. Fig. 11 displays the synthetic seismograms when varying crack densities. It is clear that reflection amplitude from the second interface increase with increasing crack density.

Table 1. Material parameters for the three-layer model as described in Chapman et al. (2006).

Lithofacies	V_P(m/s)	V_S(m/s)	ρ_W(g/cm^3)	ρ_G(g/cm^3)	φ(%)	cd(%)	Thickness(m)
Shales	2500	1250	2.02	-	-	-	1000
Shales	2743	1394	2.06	-	-	-	300
Sandstone	2835	1472	2.08	2.04	15	5,10,15,20	Half space

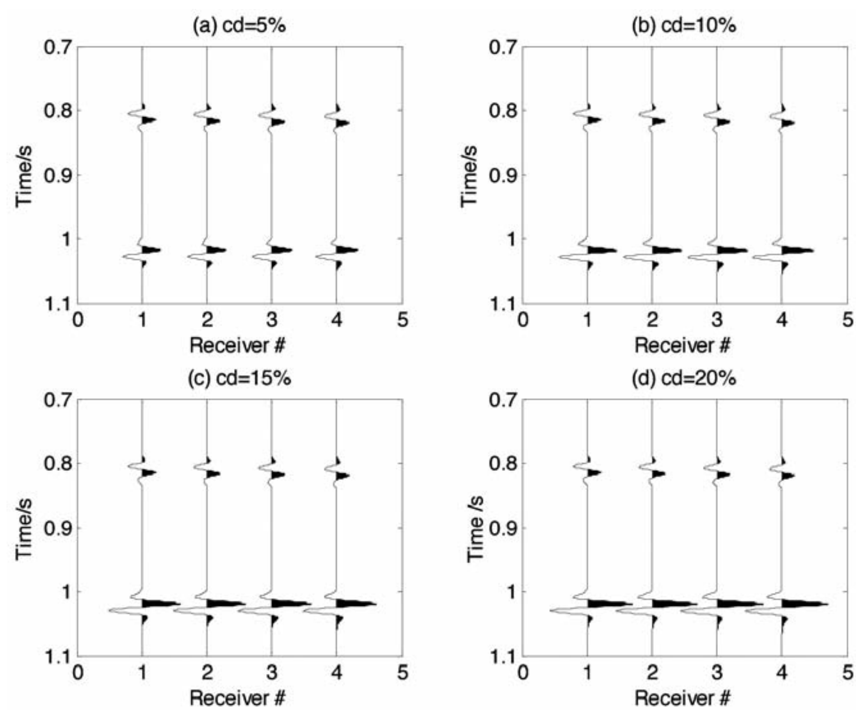

Fig. 11. Three-layer model with different crack densities.

Using the same set of frequencies at 25 Hz, 30 Hz, 40 Hz, 50 Hz, 60 Hz, 70 Hz, 80 Hz and 40 Hz as reference frequency for spectral balance, we implement FAVO attribute and obtain the I_a of the four models as shown in Fig. 12. We can find that there is no dispersion for the first interface at 0.8s, whereas there is conspicuous dispersion for the second interfaces at 1.02 s. The I_a value increases as crack density increases.

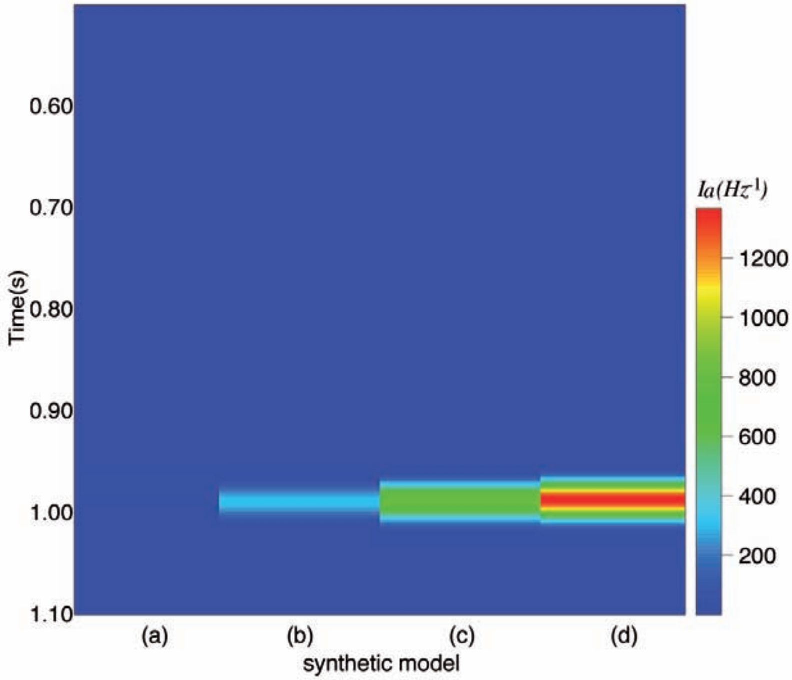

Fig. 12. The derivative of P-wave reflectivity I_a under different crack densities for the four synthetics models as displayed in Fig. 11.

CASE STUDY

Numerical test has demonstrated that the FAVO attribute scheme is able to quantitatively estimate seismic dispersion and separate dispersive models from elastic models. In this section, we present the application of FAVO attribute to real seismic data from the North Sea. Selection of optimal frequencies and reference frequency for spectral decomposition is a key issue for the calculation of FAVO attribute. To this end, we analyze the energy distribution an arbitrary pre-stack trace with Fast Fourier Transform (FFT). As shown in Fig. 13, the dominant frequency is around 15 Hz with bandwidth from 0 Hz to 40 Hz for prestack trace. We define the reference frequency f_{ref} = 15 Hz and select a set of frequencies at 10 Hz, 15 Hz, 20 Hz, 30 Hz, 40 Hz for the FAVO attribute.

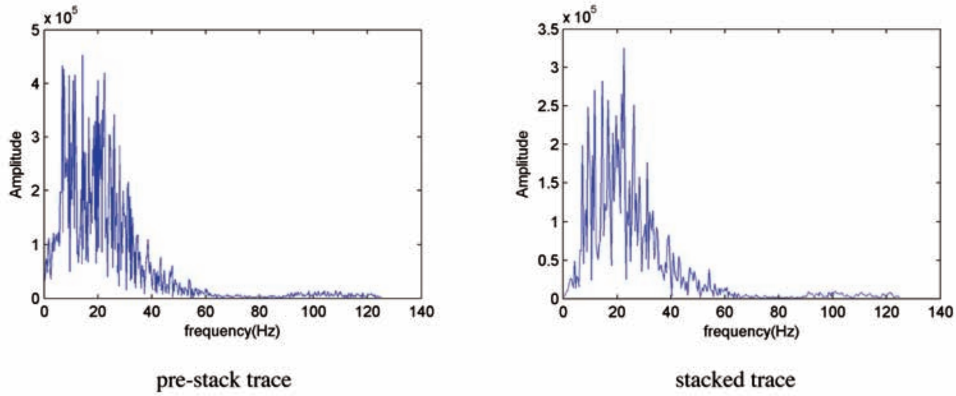

Fig. 13. Spectral analysis of a arbitrary prestack trace. (a) The whole trace. (b) Trace under 1.6 s.

Fig. 14 (a) displays the stacked section of Xline4921 from the North Sea. The target is around 2.0 s, corresponding to a relatively deep depth of about 2 km. The positions of potential reservoir exhibit as "bright spots", where the pre-stack CMP gathers have the feature of Class III AVO. We perform SPWVD on the stacked section to obtain isofrequency sections at 10 Hz, 15 Hz, 20 Hz, 30 Hz, and 40 Hz. Continuous reflections above 1.0 s can be deemed to be caused by elastic interface, therefore can be used for spectral balance with 15Hz as reference frequency. Fig. 14 (b-f) display the balanced isofrequency section at 10 Hz, 15 Hz, 20 Hz, 30 Hz, 40 Hz of the stacked section. We can see that spectral amplitudes at left and middle anomalies have a trend of increasing with frequency, whilst spectral amplitudes at the right anomaly is stable at 10 Hz, 15 Hz, 20 Hz and then decrease at 30 Hz and 40 Hz.

The pre-stack CMP gathers from No.4201 to No.5399 are extracted from the 3D seismic data for the calculation of I_a attribute. In order to reduce the influence of NMO stretching, we use the first 45 traces for the FAVO attribute.

We perform the SPWVD on each pre-stack gather to obtain isofrequency sections at 10, 15, 20, 30 and 40 Hz. A trace of I_a attribute can be calculated for each pre-stack gather. Fig. 15 displays the I_a attribute for the CMP numbers from 4201 to 5399. We can see strong reflection energy due to non-reservoir interfaces in Fig. 14 has been partially eliminated in this attribute. The zone of interest around 2.0 s shows significant magnitude of dispersion. Fig. 16 displays the No.4625 and No.4795 CMP gather. The amplitudes exhibit the typical feature of Class III AVO at the reservoir position. The inverted Ia attribute on the right shows maximum amplitude around this area, which may caused by fluids saturation.

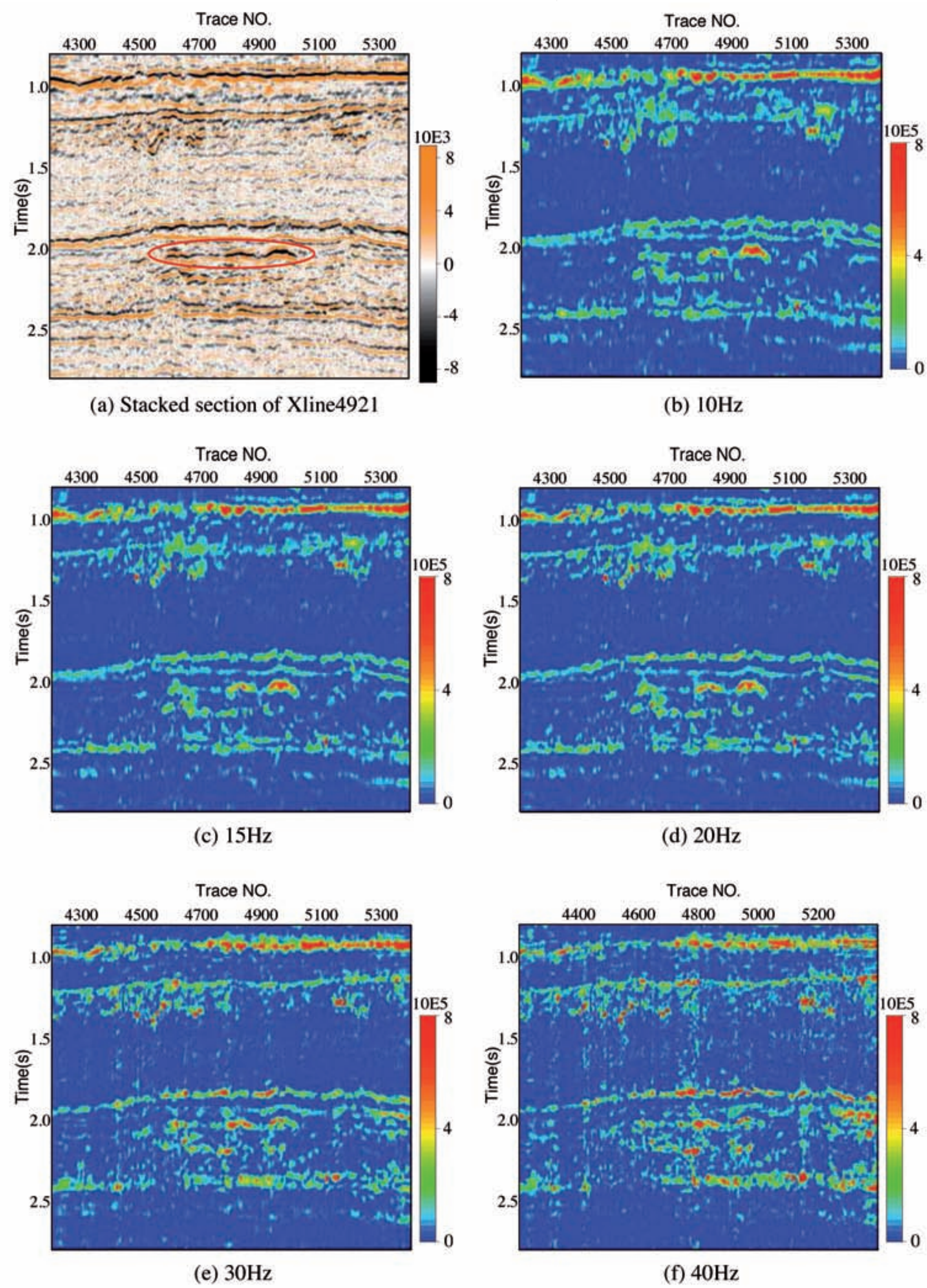

Fig. 14. The Stacked section of Xline4921 and its isofrequency sections.

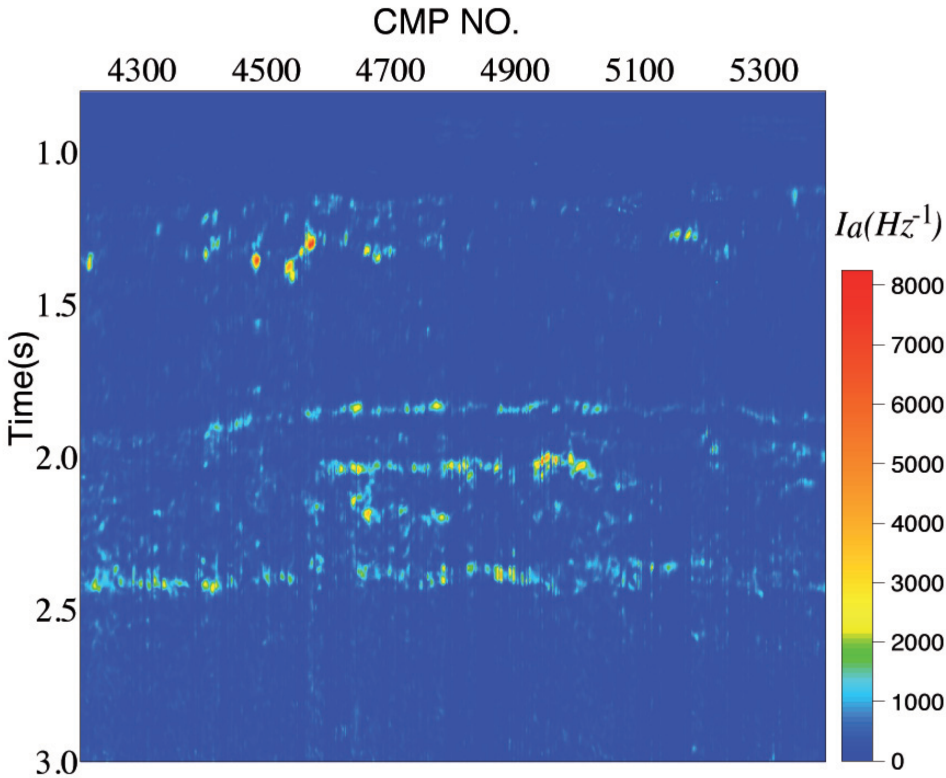

Fig. 15. The I_a attribute for the CMP number from 4201 to 5399.

CONCLUSIONS

In this paper, we have developed a FAVO attribute to demonstrate the possibility of inferring dispersion properties directly from pre-stack data and linking this to fluid saturation. The attribute combines a high-resolution spectral decomposition technique with Smith and Gidlow's (1987) AVO approximation. We illustrate the method through analysis of synthetic data. The real seismic example from the North Sea indicates the potential of this method for the detection of seismic dispersion resulting from fluid saturation.

We also compare three typical spectral decomposition techniques and use SPWVD in the FAVO attribute. forward modelling indicates that the FAVO attribute can determine the maximum magnitude of P-wave dispersion for dispersive partial gas saturation case. Higher crack density gives rise to stronger magnitude of P-wave dispersion. Real seismic data example from the North Sea suggests the potential of this method for detection of seismic dispersion due to fluid saturation.

It is worth to mention that the inversion scheme still may be affected by NMO stretching. For deep reservoirs, we use near-offset traces only in order to reduce the affect of NMO stretching, but for shallow reservoirs the NMO stretching should be corrected before inversion.

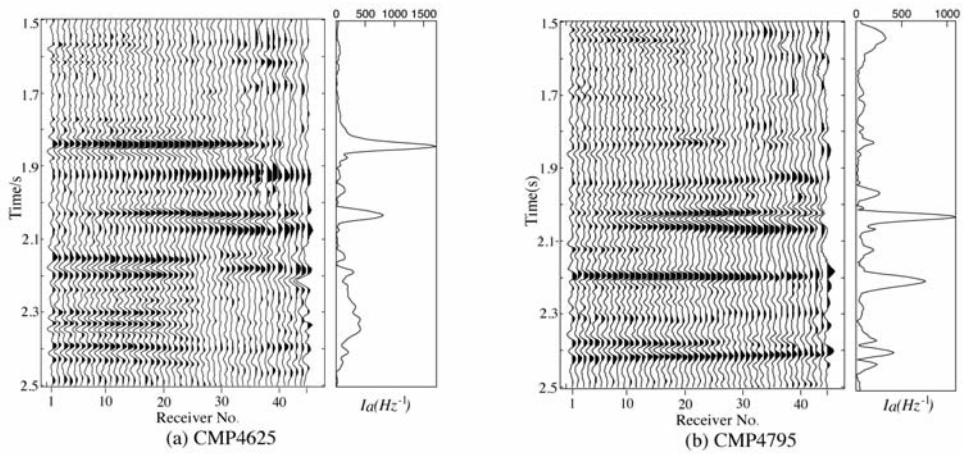

Fig. 16. The calculated Ia attribute for the two CMP gathers.

ACKNOWLEDGEMENTS

We are grateful to David Taylor for providing the code for reflectivity modelling with frequency-dependent properties (ANISEIS). This work was supported by the sponsors of the Edinburgh Anisotropy Project, British Geological Survey (NERC).

REFERENCES

Aki, K. and Richards, P.G., 1980. Quantitative Seismology. W.H. Freeman and Co., San Francisco.

Bath, M., 1974. Spectral Analysis in Geophysics. Elsevier science Publishers, Amsterdam.

Castagna, J.P., Sun, S. and Siegfried, R.W., 2003. Instantaneous spectral analysis: detection of low-frequency shadows associated with hydrocarbons. The Leading Edge, 22(3): 120-127.

Chapman, M., 2003. Frequency dependent anisotropy due to meso-scale fractures in the presence of equant porosity. Geophys. Prosp., 51: 369-379.

Chapman, M., Liu, E. and Li, X.-Y., 2006. The influence of fluid-sensitive dispersion and attenuation on AVO analysis. Geophys. J. Internat., 167: 89-105.

Claasen, T. and Mecklenbrücker, W., 1980. The Wigner distribution: a tool for time - frequency signal analysis. Philips J. Res., 35: 217-250.

Cohen, L., 1995. Time-Frequency Analysis. Prentice Hall Inc., New York.

Dasgupta, R. and Clark, R.A., 1998. Estimation of Q from surface seismic reflection data. Geophysics, 63: 2120-2128.

Gabor, D., 1946. Theory of communication. J.IEEE, 93: 429-457.

Gardner, G.H.F., Gardner, G.L. and Gregory, A.R., 1974. Formation velocity and density - The diagnostic basics for stratigraphic traps. Geophysics, 39: 770-780.

Gist, G.A., 1994. Interpreting laboratory velocity measurements in partially gas-saturated rocks. Geophysics, 59: 1100-1109.

Gurevich, B., Makarynska, D., de Paula, O. and Pervukhina, M., 2010. A simple model for squirt-flow dispersion and attenuation in fluid-saturated granular rocks. Geophysics. 75(6): N109-N120.

Hauge, P.S., 1981. Measurements of attenuation from vertical seismic profiles. Geophysics, 46: 1548-1558.

Mallat, S.G., 1999. A wavelet tour of signal processing. Academic Press Inc., New York.

Müller, T.M. and Rothert, E., 2006. Seismic attenuation due to wave-induced flow: Why Q in random structures scales differently. Geophys. Res. Lett., 33: L16305.

Murphy, W.F., 1982. Effects of partial water saturation on attenuation in massilon sandstone and vycor porous glass. J. Acoust. Soc. Am., 71: 1458-1468.

Quan, Y. and Harris, J.M., 1997. Seismic attenuation tomography using the frequency shift method. Geophysics, 62: 895-905.

Quintal, B. and Tisato, N., 2013. Modeling seismic attenuation due to wave-induced fluid flow in the mesoscopic scale to interpret laboratory measurements. 5th Biot Conf. Poromechanics, Vienna: 31-40.

Sinha, S., Routh, P.S., Anno, P.D. and Castagna, J.P., 2005. Spectral decomposition of seismic data with continuous wavelet transform. Geophysics, 70(6): 19-25.

Smith, G.C. and Gidlow, P.M., 1987. Weighted stacking for rock property estimation and detection of gas. Geophys. Prosp., 35: 993-1014.

Taner, M.T. and Treitel, S., 2003. A robust method for Q estimation. Expanded Abstr., 73rd Ann. Internat. SEG Mtg., Dallas: 710-713.

Tonn, R., 1991. The determination of seismic quality factor Q from VSP data: A comparison of different computational methods. Geophys. Prosp., 39: 1-27.

White, J.E., 1975. Computed seismic speeds and attenuation in rocks with partial gas saturation. Geophysics, 40: 224-232.

Wilson, A., Chapman, M.,and Li, X.-Y., 2009. Frequency-dependent AVO inversion. Expanded Abstr., 79th Ann. Internat. SEG Mtg., 28: 341-345.

Wilson, A., 2010. Theory and Methods of Frequency-Dependent AVO Inversion. Ph.D. Thesis, University of Edinburgh, Edinburgh.

Wu, X. and Liu, T., 2009. Spectral decomposition of seismic data with reassigned smoothed pseudo Wigner-Ville distribution. J. Appl. Geophys., 68: 386-393.

Wu, X., Chapman, M., Wilson, A. and Li, X.-Y., 2010. Estimating seismic dispersion from pre-stack data using frequency-dependent AVO inversion. Expanded Abstr., 80th Ann. Internat. SEG Mtg., Denver, 29: 341-345.